Available online at www.sciencedirect.com
ScienceDirect
Coastal Engineering 54 (2007) 811–824
Coastal Engineering
An International Journal for Coastal, Harbour and Offshore Engineers
www.elsevier.com/locate/coastaleng

An efficient mode-splitting method for a curvilinear nearshore circulation model

Fengyan Shi [a,*], James T. Kirby [a], Daniel M. Hanes [b]

[a] Center for Applied Coastal Research, University of Delaware, Newark, DE 19716, USA
[b] Pacific Science Center, Coastal and Marine Geology Program, USGS, 400 Natural Bridges Drive, Santa Cruz, CA 95060, USA

Received 7 July 2006; received in revised form 21 February 2007; accepted 21 May 2007
Available online 22 June 2007

Abstract

A mode-splitting method is applied to the quasi-3D nearshore circulation equations in generalized curvilinear coordinates. The gravity wave mode and the vorticity wave mode of the equations are derived using the two-step projection method. Using an implicit algorithm for the gravity mode and an explicit algorithm for the vorticity mode, we combine the two modes to derive a mixed difference–differential equation with respect to surface elevation. McKee et al.'s [McKee, S., Wall, D.P., and Wilson, S.K., 1996. An alternating direction implicit scheme for parabolic equations with mixed derivative and convective terms. J. Comput. Phys., 126, 64–76.] ADI scheme is then used to solve the parabolic-type equation in dealing with the mixed derivative and convective terms from the curvilinear coordinate transformation. Good convergence rates are found in two typical cases which represent respectively the motions dominated by the gravity mode and the vorticity mode. Time step limitations imposed by the vorticity convective Courant number in vorticity-mode-dominant cases are discussed. Model efficiency and accuracy are verified in model application to tidal current simulations in San Francisco Bight.

Keywords: Nearshore circulation model; Mode splitting; Numerical scheme; Curvilinear coordinates

1. Introduction

There is a growing need for an efficient nearshore circulation model which can be used as a hydrodynamic module in modeling of long time-scale nearshore processes such as coastal sediment transport, morphology change, nearshore pollutant transport, and the environmental coastal processes related to vegetation growth. The typical time scale for nearshore sediment transport simulations, for example, can be from months to years, even decadal time scales for geomorphic long-term processes. The period related to a coastal vegetation growth simulations typically involves at least a seasonal cycle. For simulations of these long time-scale nearshore processes, model efficiency and numerical stability become important issues.

Most of the existing nearshore circulation models reported in the literature (e.g., Svendsen et al., 2002; Yu and Slinn, 2001; Shi et al., 2003, and others) were developed under the CFL stability restriction relating the time step to the spatial discretization and to the free-surface wave speed. The CFL stability restriction may inhibit these models from being applied to long time-scale nearshore circulation with a sufficiently fine grid to resolve complex coastal geometry and nearshore flows. Therefore, seeking unconditionally stable and efficient numerical schemes for a nearshore circulation model becomes very necessary.

Nearshore circulation models are often developed based on depth-integrated and short-wave-averaged shallow water equations. The surface wave radiation stress concept is usually used as the short-wave force for generation of wave-induced phenomena such as wave set-up, set-down (Longuet-Higgins and Stewart, 1964; Bowen et al., 1968), longshore currents (Bowen, 1969; Longuet-Higgins, 1970), rip currents (Haas et al., 2003), shear waves (Sancho and Svendsen, 1998; Noyes et al., 2005) and infragravity waves (van Dongeren and Svendsen, 2000). A Quasi-3D nearshore circulation model SHORECIRC developed recently by Svendsen et al. (2002), is an efficient approach to modeling of wave-induced nearshore circulation with 3-D velocity profiles. SHORECIRC first calculates 2-D wave-induced currents based

* Corresponding author.
E-mail address: fyshi@coastal.udel.edu (F. Shi).

0378-3839/$ - see front matter © 2007 Elsevier B.V. All rights reserved.
doi:10.1016/j.coastaleng.2007.05.009

on depth-integrated and time-averaged hydrodynamic equations and then uses an analytical approach to evaluate the vertical variation in current velocities. The three-dimensional dispersion of momentum in wave-induced nearshore currents was discussed by Svendsen and Putrevu (1994). They found that the vertical structure of the currents leads to a mixing-like term in the depth-integrated along-shore momentum equation, which is analogous to the shear-dispersion mechanism found by Taylor (1953, 1954). The lateral mixing caused by the shear-dispersion mechanism is an order of magnitude larger than the turbulent lateral mixing and is thus considered to be major contributor to the total lateral mixing in the nearshore region. Smith (1997) also gave a more general derivation of the shear-dispersion mechanism using a multi-mode analysis of shallow water equations. Later studies on shear waves (Sancho and Svendsen, 1998; Zhao et al., 2003), using the same set of equations, showed that the 3-D dispersion terms play an important role in vorticity generation and 3-D vorticity structure. The 3-D dispersion terms, however, create a significant burden on computations as shown in Putrevu and Svendsen (1999). The curvilinear version of the SHORECIRC model developed recently by Shi et al. (2003) gives rise to extra computational time because of the coordinate transformation. With the explicit schemes implemented in both the Cartesian and curvilinear versions, the SHORECIRC model is computationally expensive in large domains and long time-scale simulations.

Recently, mode-splitting techniques have been widely adopted in three-dimensional ocean models in order to improve computational efficiency (Bleck and Smith, 1990; Dukowicz and Smith, 1994; Higdon and de Szoeke, 1997; Shchepetkin and McWilliams, 2005). The basic idea of the technique is to separate the external gravity (barotropic) mode and internal gravity (baroclinic) mode equations and then solve each of them separately at appropriate time steps dictated by the respective wave speeds. The external mode equations are obtained by integrating the continuity and momentum equations vertically over the water column, and thus the mixing-like terms (also called dispersion terms) appear in the 2-D momentum equations. The external mode equations are less expensive to solve, though smaller time steps may be needed due to the fast speed of the external gravity waves. Alternatively, the external mode can be solved using an implicit method (Oberhuber, 1993) with larger time steps. The baroclinic equations governing the internal mode are more expensive to solve but can be solved at much larger time steps dictated by the slow speed of internal gravity waves. The principal advantage of this method is significant savings in computing time. However, some concerns were expressed about model stability problems that may be caused by an inexactness in the mode-splitting (Higdon and de Szoeke, 1997). If the splitting is inexact, fast motions may be present in the baroclinic equations and induce instability when large time steps are used. Higdon and de Szoeke (1997) proposed a more precise splitting of the momentum equations to solve the instability problem. Shchepetkin and McWilliams (2005) found a combination of optimal numerical algorithms for mode-splitting and designed a split-explicit hydrodynamic kernel to prevent aliasing of unresolved barotropic signals into the slow baroclinic motions so as to enhance internal mode stability.

Following the mode-splitting idea, the SHORECIRC equations can also be split into two modes, i.e., a fast mode and a slow mode. The governing equations in SHORECIRC are essentially 2-D depth-integrated shallow water equations in which the 3-D dispersion terms represent hydrodynamic mechanisms similar to those in external mode equation 3-D ocean circulation models. Although there are no baroclinic motions in the SHORECIRC model, the 3-D dispersion effect caused by the vertical non-uniformity of the currents plays a major role in dispersive mixing. The vortical motion associated with lateral mixing and radiation stresses is basically a slow motion which should be an order of magnitude slower than gravity wave motion in shallow water. Therefore, the gravity mode and the vorticity mode can be split out from the SHORECIRC equations as the fast mode and the slow mode, respectively. In contrast to the slow mode in 3-D ocean models, the dispersion terms in the vorticity mode are based on analytical formulations rather than a partial differential equation in the vertical direction. It may be solved at the same step as the gravity mode, using an implicit–explicit combined scheme. Previous studies on such a combined numerical scheme (Casulli and Zanolli, 2002) showed that the gravity mode can be easily solved using a semi-implicit or fully implicit scheme and that only a mild limitation on the time step is imposed by the explicit form of the vorticity mode. The overall numerical schemes are nearly unconditionally stable, and thus large time steps are allowed in a computation.

The efficient ADI (Alternative Directional Implicit) scheme has been widely used in solving horizontal 2-D parabolic/elliptic/hyperbolic equations. It is easy to employ in rectangular Cartesian coordinates or orthogonal curvilinear coordinates, as the directionally-split 1-D equations lead to a diagonal dominant matrix. In non-orthogonal curvilinear coordinates, the transformed equations usually include extra terms associated with the non-orthogonality of the coordinates, which may cause some difficulties in using such a implicit scheme developed for the diagonal dominant matrix. A typical example is that, after a generalized coordinate transformation for shallow water equations, the pressure gradient terms in momentum equations may include cross-directional derivatives in the new coordinates (e.g., Shi et al., 2001; Shi et al., 2003). The off-diagonal terms may become comparable in size to the diagonal terms if the coordinates cannot be aligned along and across the flow (Fischer 1978).

In dealing with the off-diagonal terms, some extended unconditionally stable ADI schemes (or fractional step schemes similar to ADI) have been derived by several authors such as McKee and Mitchell (1970) for parabolic equations or Warming and Beam (1979) for mixed hyperbolic–parabolic equations. McKee et al. (1996) recently derived an effective unconditionally stable ADI scheme for parabolic equations with mixed derivative and convective terms. Their study was motivated by the investigation of heat and mass transfer in a fluid in an elliptical shaped domain. Generalized curvilinear coordinates were used to allow the problem to be solved in a considerably simpler rectangular geometry. After the coordinate transformation, the convection/diffusion equation gets two types of extra terms caused by the non-orthogonality of the coordinates, including second-order cross derivatives and first-order advection-like terms. The transformed equation was solved using the proposed extended ADI scheme with the inclusion of the advection-like terms into the real advection terms.

In the present study, we start with the Quasi-3D nearshore circulation equations in generalized curvilinear coordinates (Shi et al., 2003). The mode-splitting technique is applied to the curvilinear equations using a conventional two-step projection method that is different from the mode-splitting method used in typical three-dimensional ocean models. The resulting time difference equation for the vorticity mode basically includes lateral mixing, 3-D dispersion, advection, bottom friction and wave forcing. It can be solved efficiently using an explicit scheme due to its slow time-varying property. The gravity-mode equations, which contain the pressure gradient terms and the correction terms from the explicit form of the vorticity mode, are further organized by substituting momentum equations into the continuity equation. The final equation becomes a single parabolic type, mixed difference–differential equation with respect to surface elevation. The parabolic equation in curvilinear coordinates includes second order mixed derivative terms and advection-like terms. McKee et al.'s. (1996) scheme is modified and used in solving the equation.

To examine model convergence after the mode-splitting, we test convergence rates with grid refinement and time step refinement in two typical cases. The first case is the evolution of waves in a rectangular basin, which may represent gravity-mode-dominant motions. The convergence rates are tested in different ranges of Courant numbers. The second case is shear waves on a plane beach (Allen et al., 1996; Özkan-Haller and Kirby, 1999), which represents motions dominated by the vorticity mode. A limitation for use of large time steps in shear wave simulations is investigated. Finally, the model efficiency and accuracy are tested in a practical application to tidal current simulations in San Francisco Bight. We use different Courant numbers in the simulations and compare the model results with field measurements.

2. Mode splitting

The SHORECIRC equations (Putrevu and Svendsen, 1999) can be written in terms of contravariant components as (Shi et al., 2003)

$$\frac{\partial \xi}{\partial t}+\frac{1}{J}\frac{\partial}{\partial x_\alpha}(JQ^\alpha h)=0 \qquad (1)$$

$$\frac{\partial Q^\alpha}{\partial t}+\left(Q^\alpha Q^\beta\frac{Q^\beta}{h}+A_{\alpha\beta\delta}\frac{Q^\delta}{h}\right)_{,\beta}+\frac{1}{\rho}\left(S^{\alpha\beta}+\rho M_{\alpha\beta}\right)_{,\beta}$$
$$+ghg^{\beta\alpha}\frac{\partial \xi}{\partial x_\beta}+\frac{\tau^\alpha_B}{\rho}-\frac{\tau^\alpha_S}{\rho}+\left[T^{\alpha\beta}-\left(D_{\delta\beta}Q^\alpha_{,\delta}+D_{\delta\alpha}Q^\beta_{,\delta}\right)\right]_{,\beta}$$
$$-\left(B_{\alpha\beta}Q^\delta_{,\delta}\right)_{,\beta}=0 \qquad (2)$$

where Q^α and ξ represent contravariant component of depth-integrated, short-wave-averaged horizontal flux and short-wave-averaged surface elevation, respectively. $S^{\alpha\beta}$, τ^α_B, τ^α_S, and $T^{\alpha\beta}$ are radiation stresses, the bottom frictional stress, wind stress, and lateral shear stresses. $g^{\alpha\beta}$ represents the metric tensor defined by

$$g^{\alpha\beta}=\frac{\partial X\gamma}{\partial x_\alpha}\frac{\partial X\gamma}{\partial x_\beta} \qquad (3)$$

where X_γ represents horizontal spatial variables in rectangular Cartesian coordinates. The 3-D dispersion effect caused by the vertical variation of horizontal velocity is represented in the terms containing the coefficients A, B, D and M (refer to Shi et al., 2003 for details).

Eq. (2) can be split using the two-step projection method and can be approximated as follows:

$$Q^{\alpha(*)}=Q^{\alpha(n)}+\Delta tF_v^{\alpha(n)} \qquad (4)$$

$$Q^{\alpha(n+1)}=-gh\Delta tg^{\beta\alpha}\left(\frac{\partial \xi}{\partial x_\beta}\right)^{(n+1)}+Q^{\alpha(*)} \qquad (5)$$

where $Q^{\alpha(*)}$ is the intermediate flux value computed from incremental changes resulting from the vorticity mode and F_v^α represents terms dominating the vorticity mode and is given by

$$F_v^\alpha=-\left(\frac{Q^\alpha Q^\beta}{h}+\frac{A_{\alpha\beta\delta}Q^\delta}{h}\right)_{,\beta}-\frac{1}{\rho}\left(S^{\alpha\beta}+\rho M_{\alpha\beta}\right)_{,\beta}-\frac{\tau^\alpha_B}{\rho}+\frac{\tau^\alpha_S}{\rho}$$
$$-\left[T^{\alpha\beta}-\left(D_{\delta\beta}Q^\alpha_{,\delta}+D_{\delta\alpha}Q^\beta_{,\delta}\right)\right]_{,\beta}-\left(B_{\alpha\beta}Q^\delta_{,\delta}\right)_{,\beta}. \qquad (6)$$

Here, we assume the wave force and the variables associated with wave–current interaction are slowly varying. The 3-D dispersion terms containing the coefficients A, B, D and M are evaluated using the analytical formulations given in Shi et al. (2003) with the known values at the previous time step. The turbulence-induced lateral mixing $T^{\alpha\beta}$ and the bottom stress term τ^α_B are also evaluated using the known values at the previous time level. It should be mentioned that the bottom friction term could be moved to the gravity mode and solved implicitly in order to improve the numerical stability (Leendertse and Gritton, 1971). In the present study, we still keep the friction term in the vorticity mode in order to incorporate short-wave effects into the bottom friction (Svendsen et al., 2002). We do not find any numerical stability problems in our model tests.

Eq. (5) presents the gravity mode of the equations with the correction from the vorticity mode. We now call Eq. (5) the gravity mode since $Q^{\alpha(*)}$ is a known value obtained from the previous time step. Substituting Eq. (5) into the continuity Eq. (1) yields a mixed difference–differential equation,

$$\frac{\partial \xi}{\partial t}=\frac{1}{J}\frac{\partial}{\partial x_\alpha}\left(gh\Delta tJg^{\beta\alpha}\frac{\partial \xi^{(n+1)}}{\partial x_\beta}\right)-\frac{1}{J}\frac{\partial JQ^{\alpha(*)}}{\partial x_\alpha} \qquad (7)$$

or

$$\frac{\partial \xi}{\partial t}=\frac{1}{J}\frac{\partial}{\partial x_\alpha}\left(gh\Delta tJg^{\beta\alpha}\frac{\partial \xi^{(n+1)}}{\partial x_\beta}\right)-\frac{1}{J}\frac{\partial J\left(Q^{\alpha(n)}+\Delta tF_v^{\alpha(n)}\right)}{\partial x_\alpha}. \qquad (8)$$

Eq. (8) is a single parabolic equation with respect to the surface elevation at the $(n+1)$ time level. When it is solved the volume flux at time level $(n+1)$ can be calculated using Eq. (5) or

$$Q^{\alpha(n+1)} = -gh\Delta t g^{\beta\alpha}\left(\frac{\partial \xi}{\partial x_\beta}\right)^{(n+1)} + Q^{\alpha(n)} + F_v^{\alpha(n)}\Delta t. \tag{9}$$

It should be noted that Eq. (8) contains both the gravity mode and vorticity mode. The gravity mode appears in implicit form while the vorticity mode appears explicitly.

3. Numerical schemes

In order to use McKee et al.'s (1996) ADI scheme for parabolic equations with mixed derivative and convective terms, we rewrite Eq. (8) in a general form as

$$\frac{\partial \xi}{\partial t} = a_{\alpha\beta}\frac{\partial^2 \xi}{\partial x_\alpha x_\beta} + b_\alpha \frac{\partial \xi}{\partial x_\alpha} + c \tag{10}$$

where

$$a_{\alpha\beta} = gh\Delta t g^{\alpha\beta} \tag{11}$$

$$b_\alpha = \frac{g\Delta t}{J}\left(\frac{\partial J g^{\alpha\beta} h}{\partial x_\beta}\right) \tag{12}$$

$$c = -\frac{1}{J}\frac{\partial J\left(Q^{\alpha(n)} + \Delta t F_v^{\alpha(n)}\right)}{\partial x_\alpha}. \tag{13}$$

$a_{\alpha\beta}$ is a symmetric array, and thus the mixed derivative terms in Eq. (10) can be written as

$$2a_{12}\frac{\partial^2 \xi}{\partial x_1 \partial x_2}$$

or

$$2a_{21}\frac{\partial^2 \xi}{\partial x_1 x_2}.$$

Compared to the general partial differential equation given in McKee et al. (1996), Eq. (10) has an extra term c which can be treated as a source term in the advection–diffusion equation. In addition, there is no real advection term in the equation aside from the advection-like term induced by the coordinate distortion. We follow McKee et al.'s (1996) method to derive the ADI scheme and get a similar scheme for Eq. (10). To get the order of accuracy $O(\Delta t, \Delta x_\alpha^2)$, we discretize the equation on a uniform spatial mesh in the image plane with $\Delta x_1 = \Delta x_2$ and use a central difference scheme for the advection-like terms. A staggered Arakawa 'C' grid (Arakawa and Lamb, 1977) as shown in Fig. 1 is used for surface elevation and current flux. The difference equations of Eq. (10) in the alternating direction implicit schemes can be written as

$$\left[1 - \frac{ra_{11}}{2}\delta_{x_1}^2 - \frac{pb_1}{2}\nabla_{x_1}\right]\xi_{i,j}^{(n+1)^*} = \left[1 + ra_{22}\delta_{x_2}^2 + pb_2\nabla_{x_2} + \frac{ra_{11}}{2}\delta_{x_1} + \frac{pb_1}{2}\nabla_{x_1} + \frac{ra_{22}}{4}\delta_{x_1x_2}\right]\xi_{i,j}^n + \frac{\Delta t}{2}c \tag{14}$$

$$\left[1 - \frac{ra_{22}}{2}\delta_{x_2}^2 \frac{pb_2}{2}\nabla_{x_2}\right]\xi_{i,j}^{n+1} = \xi_{i,j}^{(n+1)*} - \left[\frac{ra_{22}}{2}\delta_{x_2}^2 + \frac{pb_2}{2}\nabla_{x_2}\right]\xi_{i,j}^n \tag{15}$$

where r and p are ratios defined by

$$r = \Delta t/(\Delta x_1)^2 = \Delta t/(\Delta x_2)^2, \qquad p = \Delta t/(2\Delta x_1) = \Delta t/(2\Delta x_2)$$

and we define the discretization operations

$$\nabla_{x_1}\xi_{i,j}^n = \xi_{i+1,j}^n - \xi_{i-1,j}^n$$

$$\nabla_{x_2}\xi_{i,j}^n = \xi_{i,j+1}^n - \xi_{i,j-1}^n$$

$$\delta_{x_1}^2\xi_{i,j}^n = \xi_{i+1,j}^n - 2\xi_{i,j}^n + \xi_{i-1,j}^n$$

$$\delta_{x_2}^2\xi_{i,j}^n = \xi_{i,j+1}^n - 2\xi_{i,j}^n + \xi_{i,j-1}^n$$

$$\delta_{x_1x_2}\xi_{i,j}^n = \xi_{i+1,j+1}^n - \xi_{i+1,j-1}^n - \xi_{i-1,j+1}^n + \xi_{i-1,j-1}^n.$$

The scheme is the same as that in McKee et al. (1996) except that the first-order derivatives are treated by a central difference. McKee et al. (1996) mentioned that the order of accuracy decays to $O(\Delta t, \Delta x_\alpha)$ when the first-order up-winding scheme is used for advection terms. Introducing the second order up-winding scheme can increase to $O(\Delta t, \Delta x_\alpha{}^2)$. We do not use the suggested

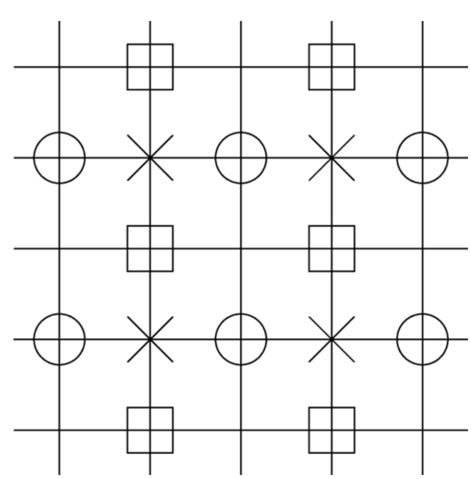

Fig. 1. Staggered Arakawa 'C' grid in x_1–x_2 plane (cross — ξ point, circle — Q^1 point, box — Q^2 point).

scheme because of the fact that the first-order derivatives in our equation are not the real advection terms. The grid distortion caused advection-like terms are expected to have minor effect on overall model accuracy under the condition of a smooth curvilinear grid.

To facilitate the description of the boundary condition implementation shown in next subsection, we give an extended form of the difference equations. Eq. (13) can be written in a tri-diagonal form as

$$d_1 \zeta_{i-1,j}^{(n+1)*} + d_2 \zeta_{i,j}^{(n+1)*} + d_3 \zeta_{i+1,j}^{(n+1)*} = d_4 \tag{16}$$

where

$$d_1 = -\frac{ra_{11}}{2} + \frac{pb_1}{2} \tag{17}$$

$$d_2 = 1 + ra_{11} \tag{18}$$

$$d_3 = -\frac{ra_{11}}{2} - \frac{pb_1}{2} \tag{19}$$

$$\begin{aligned} d_4 = {} & (ra_{22} - pb_2)\zeta_{i,j-1}^n + (ra_{22} - pb_2)\zeta_{i,j+1}^n \\ & +(1 - 2ra_{22} - ra_{11})\zeta_{i,j}^n + \left(\frac{ra_{11}}{2} - \frac{pb_1}{2}\right)\zeta_{i+1,j}^n \\ & +\left(\frac{ra_{11}}{2} + \frac{pb_1}{2}\right)\zeta_{i+1,j}^n + \frac{ra_{11}}{4}\zeta_{i+1,j+1}^n - \frac{ra_{11}}{4}\zeta_{i+1,j-1}^n \\ & -\frac{ra_{11}}{4}\zeta_{i-1,j+1}^n + \frac{ra_{11}}{4}\zeta_{i-1,j-1}^n - p(Q_{i+1,j}^{1(n)} - Q_{i,j}^{1(n)} + Q_{i,j+1}^{2(n)} \\ & -Q_{i,j}^{2(n)} + \Delta t(F_v^1)_{i+1,j}^n - \Delta t(F_v^1)_{i,j}^n + \Delta t(F_v^2)_{i,j+1}^n \\ & -\Delta t(F_v^2)_{i,j}^n) - p\left(\frac{Q_{i+1,j}^{1(n)} + Q_{i,j}^{1(n)}}{4J_{i,j}}(J_{i+1,j} - J_{i-1,j}) \right. \\ & \left. + \frac{Q_{i,j+1}^{2(n)} + Q_{i,j}^{2(n)}}{4J_{i,j}}(J_{i,j+1} - J_{i,j-1})\right) \end{aligned} \tag{20}$$

Eq. (15) can be written as

$$e_1 \zeta_{i,j-1}^{(n+1)} + e_2 \zeta_{i,j}^{(n+1)} + e_3 \zeta_{i,j+1}^{(n+1)} = e_4 \tag{21}$$

with a corresponding definition for e_1, e_2, e_3 and e_4. Eqs. (16) and (21) constitute linear tri-diagonal systems of equations for $\zeta^{(n+1)*}$ and $\zeta_{i,j}^{(n+1)}$, respectively and can be solved efficiently using elimination method with proper boundary conditions. Once $\zeta_{i,j}^{(n+1)}$ is achieved at every elevation point, the current flux $Q^{\alpha(n+1)}$ can be obtained immediately using Eq. (9) at current flux points.

4. Boundary conditions

There are several types of boundary conditions implemented in the SHORECIRC model. The use of the mode-splitting and the implicit numerical scheme requires some changes in boundary condition implementations. Here we concentrate on three frequently used boundary conditions: flux, elevation, and periodic lateral boundaries.

4.1. Specified flux boundary condition

A specified flux boundary condition in generalized curvilinear coordinates can be easily expressed by using the contravariant component of current flux:

$$Q^1 = Q_0^1 \quad \text{at west or east boundaries} \tag{22}$$

$$Q^2 = Q_0^2 \quad \text{at south or north boundaries} \tag{23}$$

where $Q_0^{\alpha}(\alpha=1,2)$ represents given depth-integrated flux values at boundaries. The case of an impermeable wall boundary is represented by the special case $Q_0^{\alpha}=0$. On a staggered grid, only flux points are arranged at the boundaries where the specified flux boundary conditions (22) and (23) are satisfied, e.g., Q^1-points at east or west boundaries and Q^2-points at south or north boundaries. Substituting the boundary conditions (22) and (23) in Eqs. (9) and (10) results in some changes in the coefficients (d_1, d_2, d_3, d_4) or (e_1, e_2, e_3, e_4) at the boundary points. At the west boundary points,

$$d_1 = 0 \tag{24}$$

$$d_2 = 1 + \frac{1}{2} ra_{11} \tag{25}$$

$$d_3 = -\frac{ra_{11}}{2} - \frac{pb_1}{2} \tag{26}$$

$$\begin{aligned} d_4 = {} & (ra_{22} - pb_2)\zeta_{i,j-1}^n + (ra_{22} - pb_2)\zeta_{i,j+1}^n \\ & +(1 - 2ra_{22} - ra_{11})\zeta_{i,j}^n + \frac{ra_{11}}{2}\zeta_{i+1,j}^n + \frac{ra_{11}}{4}\zeta_{i+1,j+1}^n \\ & -\frac{ra_{11}}{4}\zeta_{i+1,j-1}^n - p\Big(Q_{i+1,j}^{1(n)} - Q_0^1 + Q_{i,j+1}^{2(n)} - Q_{i,j}^{2(n)} \\ & +\Delta t(F_v^1)_{i+1,j}^n + \Delta t(F_v^2)_{i,j+1}^n - \Delta t(F_v^2)_{i,j}^n\Big) \\ & -p\left(\frac{Q_{i+1,j}^{1(n)} + Q_0^1}{4J_{i,j}}(J_{i+1,j} - J_{i,j}) \right. \\ & \left. + \frac{Q_{i,j+1}^{2(n)} + Q_{i,j}^{2(n)}}{4J_{i,j}}(J_{i,j+1} - J_{i,j-1})\right). \end{aligned} \tag{27}$$

Corresponding changes in (d_1, d_2, d_3, d_4) can be made for the east boundaries and changes in (e_1, e_2, e_3, e_4) for the south and north boundaries.

4.2. Specified surface elevation boundary condition

On a staggered gird, only surface elevation points are distributed at the specified elevation boundaries. Substituting the elevation boundary condition

$$\zeta = \zeta_0 \tag{28}$$

into Eq. (16) for east or west boundaries or Eq. (21) for south or north boundaries directly yields the new tri-diagonal coefficients: at the west boundaries, for example, we get $d'_1=0$, $d'_2=d_2$, $d'_3=d_3$, and $d'_4=d_4-d_1\zeta_0$ where $(\,)'$ represents new coefficients.

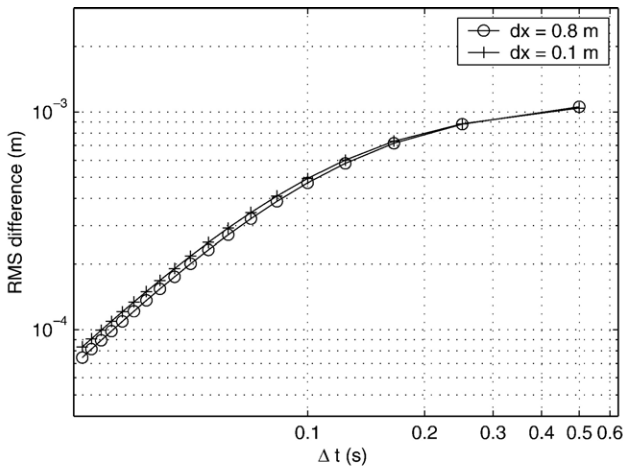

Fig. 2. RMS differences with time refinement using two different grid spacings.

4.3. Periodic boundary condition

For spatially periodic boundary conditions, only surface elevation points are defined at the boundaries. Linear periodic tri-diagonal systems can be constructed using Eq. (16) for the east–west periodic boundary and Eq. (21) for the south–north periodic boundary. For applications using the periodic boundary conditions, wave forcing, bathymetry, computational grid and other spatial distributed variables should also have the periodic properties related to the periodic boundary conditions.

5. Model applications

5.1. Tests on convergence rates in a gravity-mode-dominant case

McKee et al. (1996) used the traditional von Neumann method to prove that the scheme is unconditionally stable when the coefficients in the parabolic equation are constant. Most recently, in't Hout and Welfert (2007) derived new linear stability results for ADI schemes applied to general parabolic convection–diffusion equations with mixed derivative terms. They also showed that the ADI schemes with cross-derivative discretizations are unconditionally stable. Convergence rates with time refinement were also investigated in their study. As a specific application of this kind of ADI schemes, the discretized equations in our study need to be tested on convergence rates with both time and grid refinement. The convergence rates with grid refinement are especially important for our model since variable grid spacing is used in a grid system.

Following Shi et al. (2001), we perform simple tests of the evolution of waves in a rectangular basin. The conditions used in the numerical experiments are the same as in Shi et al. (2001), including a basin dimension of 20×20 m, 0.5 m water depth and a motionless Gaussian bump as the initial condition. To test the convergence with time discretization, we use a sequence of time steps, i.e., $\Delta t/i$, where $\Delta t=0.5$ and $i=1, 2,\ldots, 20$. We choose two different grid spacings, i.e., $\Delta x=0.1$ m and 0.8 m, for all the time steps. The convergence rates with time refinement are demonstrated by the RMS differences of simulated surface elevations at $t=20$ s. The RMS difference of surface elevation is defined by

$$\mathrm{RMS}_p=\sqrt{\frac{\sum\left(\tilde{\xi}_p(i,j)-\tilde{\xi}_{p+1}(i,j)\right)^2}{(m\times n)^2}} \tag{29}$$

where $\tilde{\zeta}_p$ represents the calculated surface elevations in the case p and (m, n) are the grid dimensions. Fig. 2 shows the RMS differences, from which the time convergence may be calculated. To evaluate convergence rates, we apply the Cauchy convergence rate defined by the following formula to convergence measurements in all cases.

$$R=\frac{\log\quad\left(\mathrm{RMS}_p/\mathrm{RMS}_{p+1}\right)}{\log\quad\left(\Delta x_p/\Delta x_{p+1}\right)}. \tag{30}$$

The averaged convergence rates for $\Delta x=0.1$ and 0.8 are 2.737 and 2.843, respectively. Fig. 2 also shows that the convergence rates for the two different grid spacings are very close. Grid spacing does not affect time convergence rates very much, which is consistent with the results of in't Hout and Welfert (2007).

To test the grid convergence at different time steps, we choose a series of time steps, i.e., $\Delta t=0.01$, 0.1, 0.3 and 0.5 s. A sequence of different grid spacing $\Delta x/(p_m-p)$, where $\Delta x=0.8$ m, $p_m=9$ and $p=1, 2, 3,\ldots, 8$, are adopted for each Δt. The range of Courant Numbers are from $C_r=0.006$ for the case of $\Delta t=0.01$ s and $p=8$ to $C_r=2.26$ for $\Delta t=0.5$ s and $p=1$. Fig. 3 shows the RMS differences with grid refinement at different time steps. The RMS difference of surface elevation is also calculated by Eq. (29) with (m, n) as the grid dimensions in the case of $p=8$. It is found that, in the cases with smaller time steps, the logarithmic RMS differences vary linearly with respect to the logarithmic grid spacing. The convergence tends to be slower as larger time steps are adopted. The averaged Cauchy convergence rates are 2.66, 2.25, 1.83, and 1.42 for the cases of $\Delta t=0.01$, 0.1, 0.3, and 0.5 s, respectively. Compared to a value of 3.58 obtained from the same case in Shi et al. (2003), the averaged convergence rate (2.66) from the present test with $\Delta t=0.01$ is a little bit smaller because only second order schemes are utilized in the model.

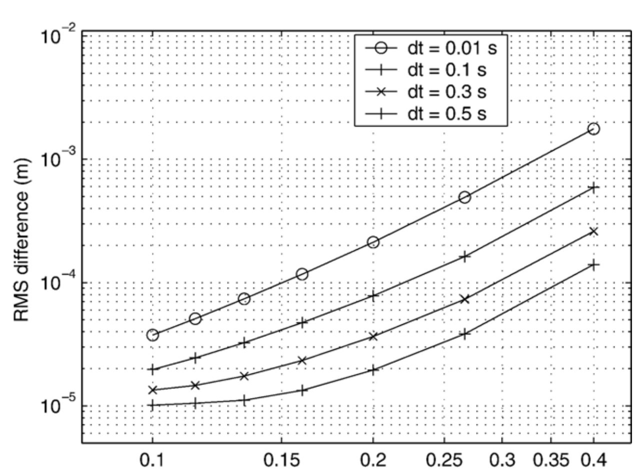

Fig. 3. RMS differences with grid refinement using different time steps.

In the development of the fully non-linear Boussinesq models (Wei and Kirby, 1995; Shi et al., 2001), higher-order numerical schemes in both space and time were used because the truncation errors of a second-order approximation may contaminate the real dispersive terms in the Boussinesq equations. This should not be a problem in the present model because the SHORECIRC equations do not include terms involving higher-order derivatives. However, it should be noted that the present numerical schemes, with first-order accuracy in time and second order accuracy in space, may cause numerical diffusion that may affect calculations of physical diffusion caused by turbulent mixing. To examine the accuracy of the second-order ADI schemes, we make a numerical test against the previous explicit scheme which is second-order in time and fourth-order in space (Shi et al., 2003). The previous model with the higher-order scheme is run in the same application with $\Delta x=0.4$ m and $\Delta t=0.04$ s. The result for surface elevation is compared to the present model results with a sequence of time steps. Fig. 4 shows the averaged (over all grid points) RMS errors of surface elevation between the previous model result and results from the present model at different time steps. It shows that the accuracy of the present model with second-order schemes is lower than the previous model. But it is acceptable for regular hydrodynamic simulations. For simulations with complex geometries, the Courant numbers are suggested not to exceed 10 because of the "ADI effect" (Casulli and Cheng, 1992).

5.2. Vorticity-mode-dominant case: modeling of nearshore shear waves

Studies on surfzone dynamics have revealed the existence of a variety of low-frequency motions including edge waves, surf beat and shear waves at the shoreline (Noyes et al., 2005). Amongst these low-frequency waves are shear waves, which are manifestation of shear instability of the mean longshore current. Shear waves are dominated by vorticity dynamics and have little representation in the surface displacement signal. In numerical models, the classic approach to "lateral mixing" is to specify a priori an empirical viscosity coefficient which is either constant (e.g., Deigaard et al., 1994) or cross-shore varying (Özkan-Haller and Kirby, 1999). Svendsen and Putrevu (1994) pointed out that the 3-D dispersive mixing mentioned in Section 2 in this paper should be the major part of the lateral mixing in longshore currents. In the present numerical model, we assume that the vorticity mode associated with the lateral mixing is a slowly varying mode compared to the gravity mode, so that large time steps could be applied according to the CLF-free schemes in the gravity mode. However, because the vorticity mode becomes the dominant mode in the modeling of shear waves, the explicit form of the vorticity mode would restrict the time step used in the model. For the vorticity mode, the vorticity convective Courant number is related to the local convective velocity rather than the gravity phase speed, and is expected to limit the time step. According to the depth-averaged 2-D form of vertical vorticity transport equation (Zhao et al., 2003), the vorticity convective velocity is primarily the depth-averaged current velocity if neglecting vorticity stretching. Therefore, the convective Courant number for the vorticity mode can be approximately estimated as

$$C_{\mathrm{r}}^{\mathrm{vor}}=\frac{|\mathbf{u}|\Delta t}{\Delta x} \tag{31}$$

where $\mathbf{u}$ represents the depth-averaged current velocity. To prove our expectation, we carry out the simple test initially proposed by Allen et al. (1996) who utilized the rigid lid assumption and modeled the instability of an analytic longshore cur rent profile on a sloping beach with slope of 0.05. Özkan-Haller and Kirby (1999) repeated one of Allen et al.'s (1996) cases using general two-dimensional shallow water equations with radiation stresses as wave forcing. They found some similarities in vortex interactions between the idealized plane beach test and practical shear wave simulations associated with the SUPERDUCK field experiment. Allen et al. (1996) pointed out that, in their numerical solutions, shear wave behavior may vary over the full range from periodic to chaotic with different bottom fiction coefficients and domain size. For comparison, we conducted a shear wave simulation on a plane beach which was used by Özkan-Haller and Kirby (1999). The computational domain is set to be 350 m and 3600 m in cross-shore and along-shore directions, respectively. The grid sizes are chosen as 5 m in both directions. Wave forcing, i.e., radiation stresses, is calculated from the REF/DIF-1 wave model (Kirby et al., 2002). Periodic boundary conditions are used in the along-shore direction. We use the quadratic-type bottom stress formulation (Svendsen et al., 2002) with a constant bottom friction coefficient $f_{\mathrm{cw}}=0.003$ with which we get a vorticity pattern similar to that in Özkan-Haller and Kirby (1999). For lateral mixing, there is no specification of a lateral mixing parameter needed since the lateral mixing mainly depends on the 3-D dispersion evaluated by the local vertical profiles of the calculated current velocities. To trigger shear waves on the longshore uniform plane beach, we used the same strategy as that used in Özkan-Haller and Kirby (1999), and introduce small perturbations in the initial longshore velocity v given by

$$v(x,y,t=0)\frac{\varepsilon}{\max(f)}f, \tag{32}$$

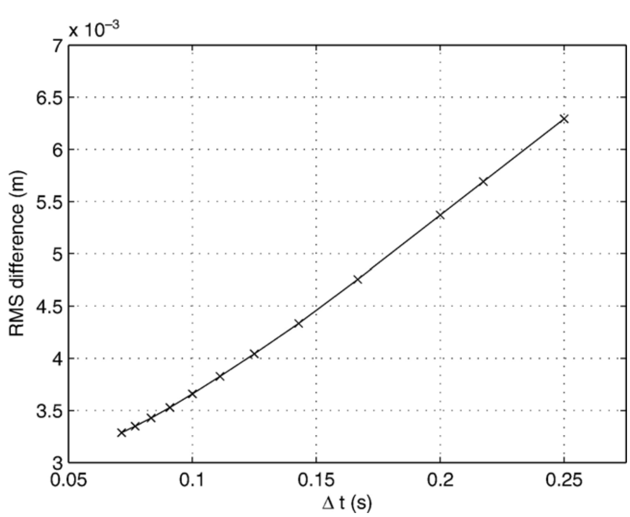

Fig. 4. Averaged RMS differences of surface elevation between models with the present second-order schemes and the previous higher-order schemes.

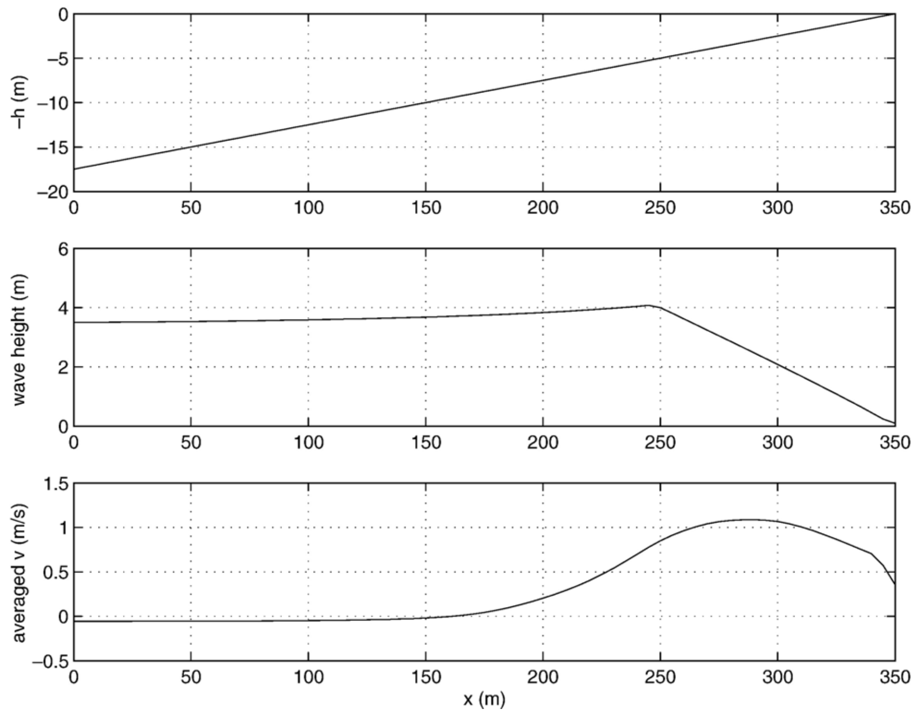

Fig. 5. Simulation of longshore currents on a plane beach. (Top) Bathymetry with a slope of 0.05, (middle) wave height from the REF/DIF-1 wave model, (bottom) longshore current profile.

where ε is a small parameter and the function f is given by

$$f = \sum_{j=1}^{\mathrm{ND}} \cos\left(\frac{2\pi jy}{L_y} + 2\pi\phi_j\right) \tag{33}$$

in which, ND is the number of times the most unstable wavelength fits into the modeling domain and ϕ_j is a random phase function between −1 and 1. L_y represents the domain length in the longshore direction. Following Özkan-Haller and Kirby (1999), we adopted ND = 16 that ensures the generations of the most unstable wavelength as well as all longer wavelengths in the modeling domain. We use $\varepsilon = 1 \times 10^{-3}$, which is orders of magnitude larger than that used in Özkan-Haller and Kirby (1999), in order to accelerate the process of shear wave generation.

Fig. 5 shows the wave height distribution predicted by the REF/DIF-1 wave model and the longshore current profile (longshore-averaged) along with the water depth h for a monochromatic wave with a frequency of 0.10 Hz and wave direction of 20 at 17.5 m water depth. It is found that the longshore-averaged current profile does not vary much when different time steps are applied. In Fig. 6, we show a snapshot of the computed wave-induced nearshore currents (arrows) and vertical vorticity (color) distribution at 180 min. Compared with the vorticity fields in Özkan-Haller and Kirby's (1999) case, the length of the shear waves and vorticity patterns look comparable to their results at the time before more vortices merge together.

We now concentrate on testing of numerical convergence in shear wave simulations using different temporal resolutions. A sequence of different time steps is selected, i.e., $\Delta t \times 2^p$, where

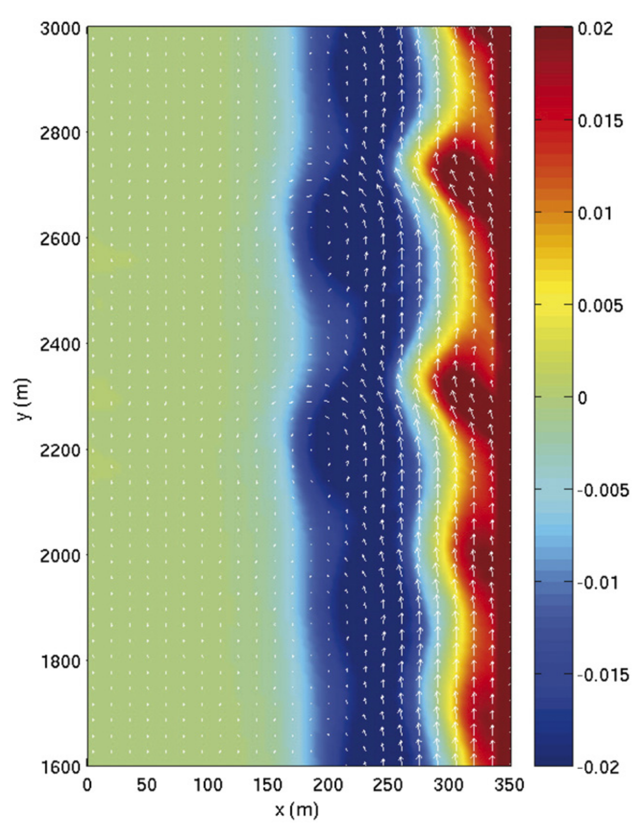

Fig. 6. Snapshot of current field (arrow) and vorticity (color, s^{-1}) for a plane beach.

Δt=0.125 s and p=0, 1,..., 6. The corresponding gravity wave Courant numbers (the maximum values in the computational domain) for the sequence of time steps are from 0.16 to 10.48 according to

$$C_r^{gra}|_{max} = \frac{\sqrt{gh_{max}}\Delta t}{\Delta x}. \tag{34}$$

The maximum Courant numbers for vorticity convection can be also evaluated based on (31):

$$C_r^{vor}|_{max} = \frac{|\mathbf{u}_{max}|\Delta t}{\Delta x} \tag{35}$$

where $\mathbf{u}_{max}$ represents the maximum current velocity vector in the whole computational domain. To characterize the strength of shear waves in the numerical results, we use the enstrophy integrated over the computational domain:

$$\Phi = \int_0^{L_x}\int_0^{L_y} \frac{\omega_z\omega_z}{2} dxdy \tag{36}$$

where ω_z is the depth-averaged vertical vorticity for shear waves. Model convergence with time discretization in the shear wave simulations can be evaluated by $\Delta\Phi=\Phi_{p+1}-\Phi_p$ with respect to Δt, C_r^{vor} or C_r^{gra}. The convergence rate with time step refinement is shown in Fig. 7 in which the gravity wave Courant numbers are labeled on the top axis while the corresponding vorticity wave Courant numbers are labeled on the bottom axis. The model is convergent with the time step refinement. The shear waves can be modeled using larger gravity wave Courant numbers, but time steps are still restrained by the vorticity wave Courant numbers. It is found that vorticity wave Courant numbers should be less than 1 in shear wave simulations using the present model, otherwise, numerical instability would occur.

5.3. Application to San Francisco Bight

In ocean-exposed coastal regions, waves, nearshore circulation and sediment transport are usually affected by large-scale motions such as tides, ocean circulation and storm surges. In modeling of nearshore processes at open coasts, open boundary conditions associated with the large-scale motions are needed by the nearshore models and are usually unknown if without measurements. It is a challenge how to incorporate far field data into nearshore models. Besides model coupling techniques performed between the nearshore models and large-scale models to apply the far field data, one efficient method is to extend the nearshore models for relatively larger scale applications. For the nearshore circulation model, for instance, the model extension can be made by approximately adding some large-scale forcing components such as tidal boundary conditions, wind stresses and the Coriolis force. The extended nearshore circulation model will become more computationally expensive because all the existing nearshore model features are included. The improvement of computational efficiency for an extended nearshore circulation model is therefore important. In the following model application to San Francisco Bight, we demonstrate the capability of the present model to simulate tidal currents and nearshore simulations in large-scale computational domains with high efficiency.

San Francisco Bight is characterized by broad shoals and narrow channels in a complicated estuary system. Because of large variations of depth distribution at the ebb tidal delta and the deep Golden Gate channel, the hydrodynamic conditions involving wave-current interaction are extremely complicated. Strong tidal currents at the entrance of the Golden Gate significantly affect wave transformation and lead to a complex, longshore-inhomogeneous wave climate which, in turn, leads to variable sediment transport processes at the inlet and nearshore regions. Recent studies on the beach evolution (Barnard et al., 2004) indicated that the shape and location of the ebb tidal shoal directly link to an erosional 'hot spot' on the southern end of Ocean Beach. Previous systematic numerical studies on hydrodynamics in San Francisco Bay have been carried out with a focus on tidal currents and residual flows inside the bay (Cheng and Casulli, 1982; Cheng et al., 1993, and others). However, nearshore hydrodynamic processes were rarely linked to the large-scale simulations.

As the first step to develop a model system predicting waves, nearshore circulations and sediment transport in the San Francisco coastal region, we concentrate on modeling tidal currents and wave-induced nearshore circulations with an aim to examine the model efficiency in such a large-scale computational domain.

Fig. 8 shows the computational grid generated using the *CoastGrid* software (Shi, 2007). The maximum grid size is 1, 320 m at the offshore boundaries. Finner grid cells are applied at the coastline and the inlet (see blow-up Fig. 9) with a minimum grid size of 19 m. The computational domain covers the whole San Francisco Bay and the adjacent Pacific shelf. Specifically, the western offshore boundary is located at the shelf edge and southern and northern boundaries are near Monterey Bay and Pt. Reyes, respectively. The tidal boundary conditions are applied at the western, southern and northern open boundaries. Eight harmonic constituents, including M_2, K_1, O_1, S_2, P_1, N_2, Q_1 and K_2, are obtained from harmonic analysis of tidal data observed at the Pt. Reyes Buoy and the Monterey Buoy. The constituents are

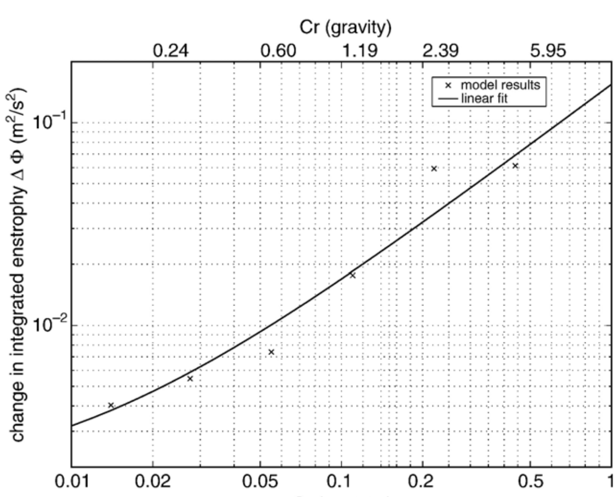

Fig. 7. Changes in integrated enstrophy with time step refinement.

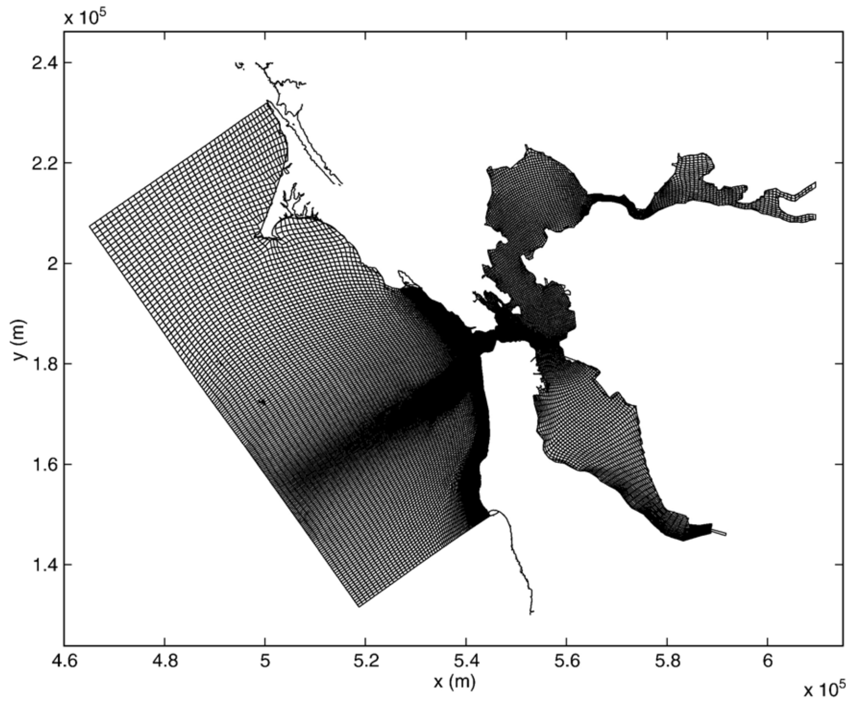

Fig. 8. Computational grid for the domain of San Francisco Bight.

used to estimate the tidal elevations at the western, northern and southern boundaries. Based on historical records, a river discharge of 400 m^3/s is specified for each of the Sacramento River and San Joaquin River located at the north-west end of the domain. Wind is taken into account using the wind data from the NOAA San Francisco station 46026 uniformly over the whole domain.

The bottom stress formulation (Svendsen et al., 2002) with a constant bottom friction coefficient $f_w = 0.0020$ is adopted in the tidal current simulation. The turbulent mixing coefficients in the eddy viscosity formulation are chosen as the same values as in Svendsen et al. (2002).

We carried out a six-month simulation of tides in which the ADCP data are available at a location in the Golden Gate

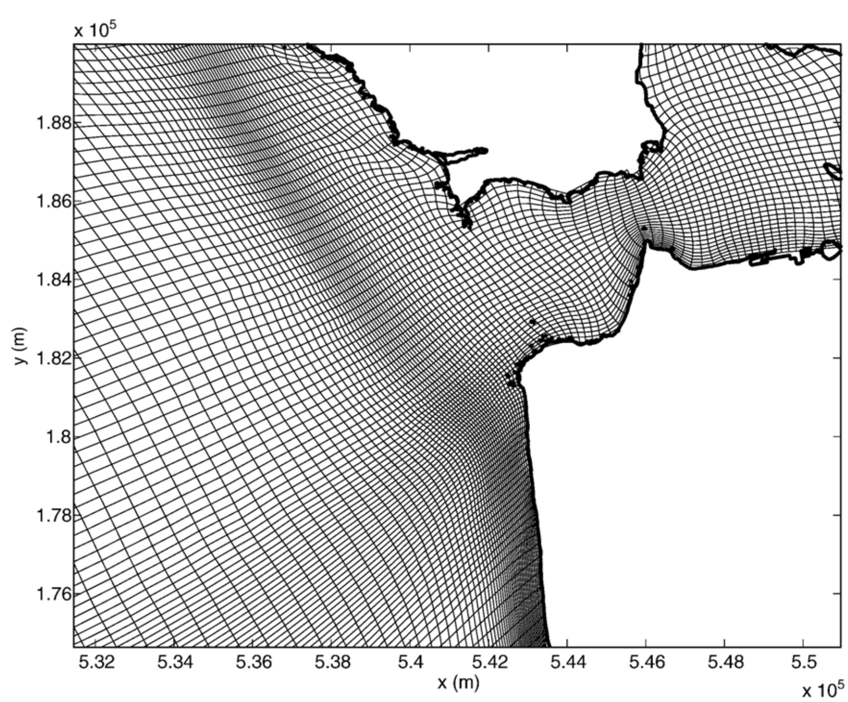

Fig. 9. Blow-up of the computational grid at the inlet and Ocean Beach.

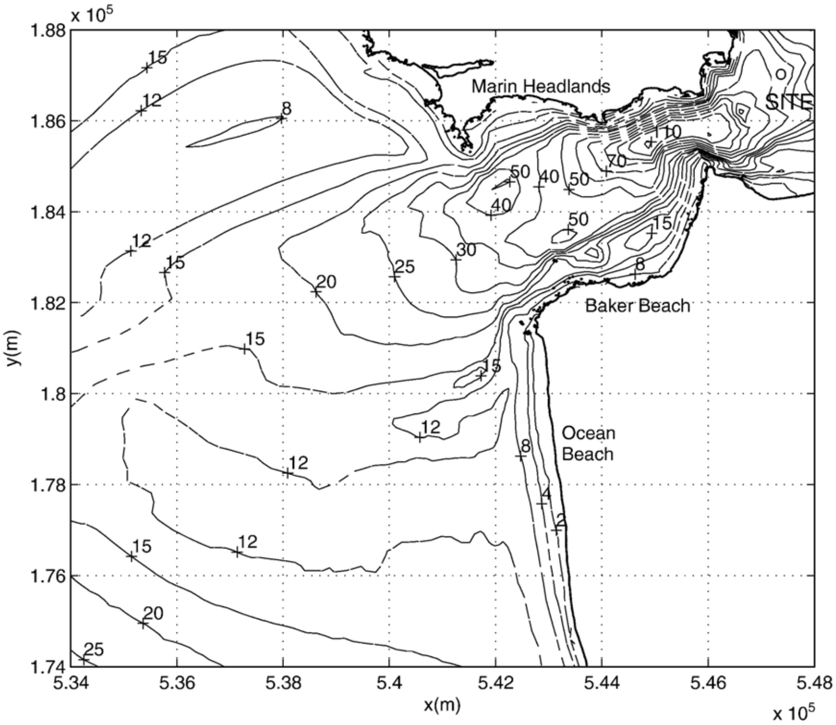

Fig. 10. Nearshore bathymetry and the measurement location (SITE).

channel as shown in Fig. 10 (marked ‘SITE’). The simulation time period is from January 1 to June 30, 1998. Different Courant numbers are used in the tests. Surface wave forcing is not taken into account in the case. It is found that the model/data comparisons of surface elevation at the Golden Gate station are satisfactory in the six-month time period except for a two-day spin-up period. Fig. 11 shows the model/data comparisons of surface elevation with Courant numbers of 10 and 100, respectively. It can be seen that the two numerical results are basically identical and both of them agree well with the data. An evaluation of the correlation between model results and data shows that the regression coefficients R^2 for surface elevation are 0.945 for $C_r = 10$ and 0.942 for $C_r = 100$. Fig. 12 shows comparisons of depth-averaged tidal currents modeled from $C_r = 10$ (solid line) and $C_r = 100$ (dashed line) against the depth-averaged ADCP data. It is shown that the tidal currents modeled from different Courant numbers are basically close, with the two line types undistinguished in the figure. The regression coefficient R^2, which is calculated using a discontinuous ADCP data of depth-averaged velocity amplitude, is 0.550 for $C_r = 100$ and 0.553 for $C_r = 10$ in the six-month time period. Figs. 13 and 14 demonstrate snapshots of tidal current fields at

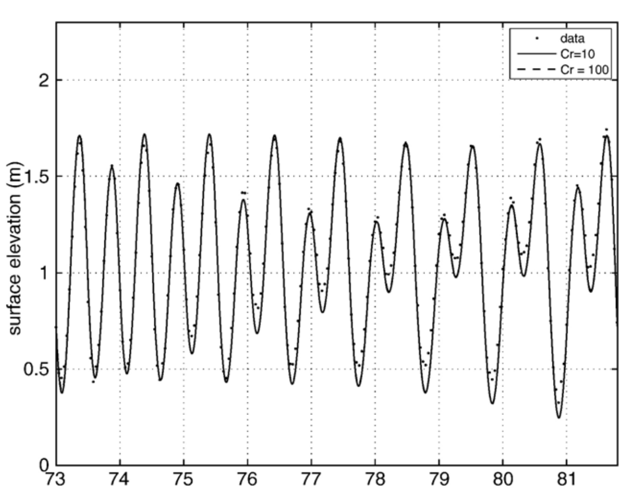

Fig. 11. Model/data comparison of surface elevations at a location (SITE) near the Golden Gate channel.

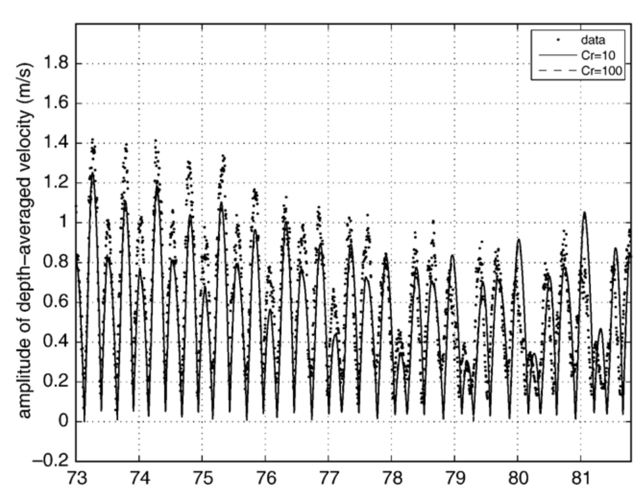

Fig. 12. Model/data comparison of depth-averaged tidal current magnitude at a location (SITE) near the Golden Gate channel.

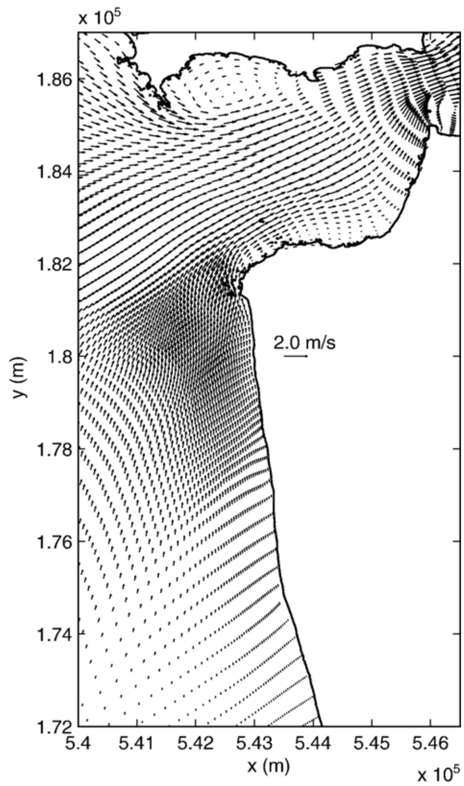

Fig. 13. Snapshot of tidal current field during flood tide.

flood tide and ebb tide, respectively. Strong tidal currents, with the maximum depth-averaged velocity of over 2 m/s, can be found at the Golden Gate channel. Several vortex cells are identified at upper Ocean Beach, Baker Beach and Marin Headlands.

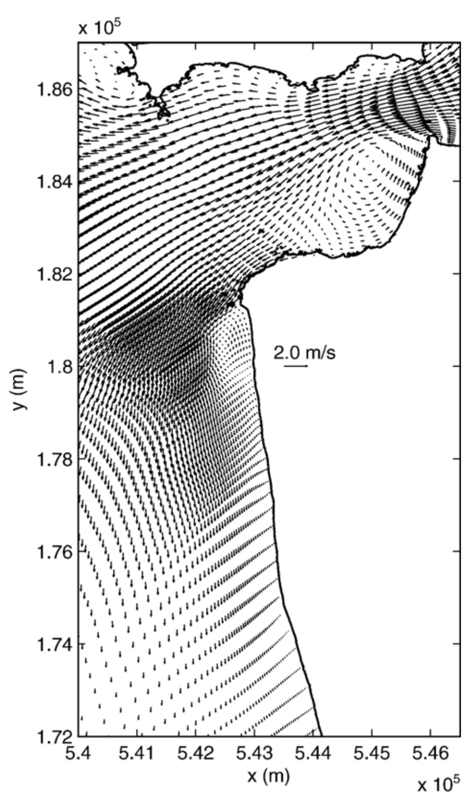

Fig. 14. Snapshot of tidal current field during ebb tide.

Wave-induced nearshore circulation can be modeled by coupling a circulation model and a wave model. In the San Francisco Bight application, we coupled the present circulation model and the spectral wave model SWAN (Booij et al., 1999). The non-stationary mode of SWAN was adopted in a two-way coupling system. As a model test, wave-induced nearshore circulation at Ocean Beach is simulated under common storm wave conditions with 3 m significant wave height, and 15 s peak period in deep water. A constant wind field with 10 m/s from 300°(Nautical) is used in the simulation. Fig. 15 shows wave-induced longshore currents along the Ocean Beach. The current magnitude is about 1 m/s which is comparable to the magnitude of tidal currents in this region.

It should be mentioned that, most recently, the U.S. Geological Survey (USGS) began a seasonal surveying campaign at Ocean Beach. Nearshore bathymetry data has been collected bi-annually, with additional surveys to coincide with instrument deployments in the offshore and surfzone regions. The SHORECIRC model with the fast numerical schemes developed in this study has been coupled with the wave model SWAN and a sediment model to investigate waves, currents and sediment transport in San Francisco Bight. The model results validated using the field data will be reported in the near future, in conjunction with a more detailed investigation of waves, nearshore circulations and sediment transport in San Francisco Bight and its adjacent open beaches.

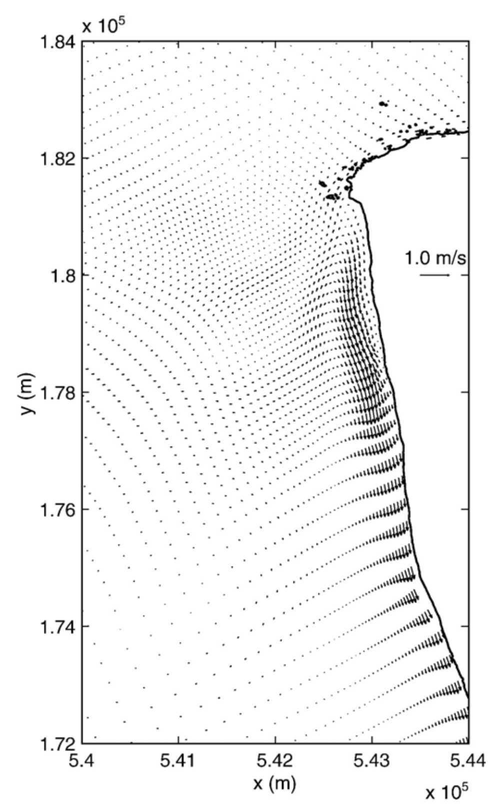

Fig. 15. Wave-induced longshore currents under incident wave conditions of 3 m significant wave height, and 15 s peak period in deep water, and 10 m/s wind from 300° over the whole domain.

6. Conclusions and remarks

A mode-splitting method is used in the Quasi-3D nearshore circulation model SHORECIRC with an aim to improve the model efficiency. Using the two-step projection method, we separate the gravity mode and the vorticity mode which represent respectively the fast motions and the slow motions in the nearshore hydrodynamic system. The vorticity mode of the equations is used to compute the intermediate flux value from incremental changes resulting from wave forcing, 3-D dispersion effect caused by the vertical non-uniformity of current velocity, the turbulence-induced lateral mixing and the bottom friction. We use an explicit scheme for the vorticity mode, especially, the 3-D dispersion terms are evaluated based on analytical formulations and using the known values of current velocity at previous time level. The gravity mode includes the pressure gradient terms, which represents incremental changes resulting from the pressure gradient. The final equation for the combination of the gravity mode and vorticity mode is derived by substituting the momentum equations into the continuity equation and it becomes a single parabolic equation with respect to surface elevation. The parabolic-type equation can be solved implicitly using the traditional ADI scheme, specifically in the present model, McKee et al.'s (1996) ADI scheme for parabolic equations is used to deal with the mixed derivative and convective terms caused by the coordinate transformation.

To test the model convergence rates with the refinement of grid spacing and time step, we carried out two typical cases, i.e., the evolution of waves in a rectangular basin which is a gravity-mode-dominant case, and the simulation of shear waves on a plane beach which is a case dominated by the vorticity mode. The case of wave evolution shows that the averaged Cauchy convergence rates with grid refinement are a little lower than the previous SHORECIRC model (Shi et al., 2003) but are still satisfactory considering the second order schemes utilized in the model. In the case of the shear wave simulation, we found that relatively larger time steps (gravity convective Courant number>1) can be used but the time steps are restricted by the explicit form of the vorticity mode. The vorticity convective Courant number that is a function of the local convective velocity rather than the gravity phase speed, limits the time steps. The test shows the model is convergent with the time step refinement and the vorticity wave Courant numbers should not exceed 1 in shear wave simulations.

Model application to San Francisco Bight indicates that the model has the capability of large-scale modeling with good efficiency. For the present application grid with dimensions of 291×180, the time step is 10.8 s for $C_r=10$ or 108 s for $C_r=100$. On a 64-bit linux system with a single processor of 2.0 GHz and a memory of 2 GB, the model with $C_r=10$ takes about 60.8 h, or about 6 h with $C_r=100$, for a 365-day simulation of tidal currents, without coupling of the wave and sediment models. With the SWAN model coupled in the system, the efficiency of the coupled model system mainly depends on the SWAN model set-up and may become computational expensive, especially when a smaller Courant number is chosen. However, it is obvious that the model efficiency is greatly improved using the present numerical schemes compared to the previous SHORECIRC model with a limitation of $C_r<1$.

The model is validated using the ADCP data measured near the Golden Gate channel in 1998. Model results of tidal surface elevations and tidal currents are in good agreements with the data. A test using different Courant numbers in the simulations shows that the Courant number can be increased to 100 without significant loss in accuracy. Finally, wave-induced longshore currents along the open beaches are calculated by coupling the present model and the wave model SWAN.

The basic hypothesis for the mode-splitting is that the nearshore motions can be separated into fast motions dominated by the gravity mode and slow motions dominated by the vorticity mode. However, nearshore processes with wave–current interactions are complex and may involve a large range of time scales. In some cases (e.g., rip current simulation using SHORECIRC, Haas et al., 2003), the time scale for the current field variation to respond to wave-current interaction may be small, which would limit the use of larger time steps in the nearshore circulation model. More tests for the time step limitation should be carried out in a wide range of nearshore applications in the future.

In the extension of the present model to large-scale applications, we neglect the baroclinic motions that may be important in estuarine or some coastal regions. Therefore, the usage of the model extension at this stage should be confined to applications in which the barotropic tides are dominant far field boundary conditions in the nearshore circulation modeling.

The CFL-free ADI scheme does not mean that large Courant numbers could be used for gravity wave motions. Because of the "ADI effect" caused by complex geometries (Casulli and Cheng, 1992), the Courant numbers were suggested not to exceed 10 to get accurate results. Although we use $C_r=100$ in the case of San Francisco Bight with a good accuracy, more numerical experiments may be needed for different geometries.

Acknowledgments

This study was supported by Office of Naval Research, Coastal Geosciences Program (N00014-05-1-0423) and U.S. Geological Survey, Coastal Evolution: Process-based Multi-scale Modeling Project.

References

Allen, J.S., Newberger, P.A., Holman, R.A., 1996. Nonlinear shear instabilities of alongshore currents on plane beaches. J. Fluid Mech. 181–213.

Arakawa, A., Lamb, V.R., 1977. Computational design of the basic dynamical processes of the UCLA general circulation model. Methods Comput. Phys., vol. 17. Academic Press, pp. 174–265.

Barnard, P.L., Hanes, D.M., Ruggiero, P., 2004. The relative effects of wave climatology and tidal currents on beach processes adjacent to a major tidal inlet, Ocean Beach, San Francisco, California, AGU, Fall Meeting 2004, San Francisco, abstract published in EOS Transaction AGU, 85 (47), Abstract OS24A-08.

Bleck, R., Smith, L.T., 1990. A wind-driven isopycnic coordinate model of the north and equatorial Atlantic Ocean 1. Model development and supporting experiments. J. Geophys. Res. 95, 3273–3285.

Booij, N., Ris, R.C., Holthuijsen, L.H., 1999. A third-generation wave model for coastal regions. Part 1: model description and validation. J. Geophys. Res. 104 (C4), 7649–7666.

Bowen, A.J., 1969. The generation of longshore currents on a plane beach. J. Mar. Res. 27, 206–215.

Bowen, A.J., Inman, D.L., Simmons, V.P., 1968. Wave set-down and set-up. J. Geophys. Res. 73, 2569–2577.

Cheng, R.T., Casulli, V., 1982. On Lagrangian residual currents with applications in South San Francisco Bay, California. Water Resour. Res. 18, 1652–1662.

Cheng, R.T., Casulli, V., Cartner, J.W., 1993. Tidal, Residual, Intertidal Mudflat (TRIM) model and its applications to San Francisco Bay, California. Estuar. Coast. Shelf Sci. 36, 235–280.

Casulli, V., Cheng, R.T., 1992. Semi-implicit finite difference methods for three-dimensional shallow water flow. Int. J. Numer. Methods Fluids 15, 629–648.

Casulli, V., Zanolli, P., 2002. Semi-implicit numerical modeling of nonhydro-static free-surface flows for environmental problems. Math. Comput. Model. 36, 1131–1149.

Deigaard, R., Christensen, E.D., Damgaard, J.S., Fredsoe, J., 1994. Numerical simulation of finite amplitude shear waves and sediment transport. 24th International Conference on Coastal Engineering, ASCE, Reston, Va.

Dukowicz, J.K., Smith, R.D., 1994. Implicit free-surface method for the Bryan–Cox–Semtner ocean model. J. Geophys. Res. 99 (C4), 7991–8014.

Fischer, H.B., 1978. On the tensor form of the bulk dispersion coefficient in a bounded skewed shear flow. J. Geophys. Res. 83, 2373–2375.

Haas, K., Svendsen, I.A., Haller, M.C., Zhao, Q., 2003. Quasi-three-dimensional modeling of rip current systems. J. Geophys. Res. 108 (C7), 3217. doi:10.1029/2002JC001355.

Higdon, R.L., de Szoeke, R.A., 1997. Barotropic-baroclinic time splitting for ocean circulation modeling. J. Comp. Phys. 135, 31–53.

in't Hout, K.J., Welfert, B.D., 2007. Stability of ADI schemes applied to convection-diffusion equations with mixed derivative terms. Appl. Numer. Math. 57, 19–35.

Kirby, J.T., Dalrymple, R.A., Shi, F., 2002. Combined refraction/diffraction model REF/DIF 1, version 2.6. Documentation and User's Manual, Research Report No.CACR-02-02, Center for Applied Coastal Research. Department of Civil and Environmental Engineering, University of Delaware, Newark.

Leendertse, J.J., Gritton, E.C., 1971. A water quality simulation model for well-mixed estuaries and coastal sea. Computation Procedures, R-708-NYC Vol II. The Rand Corporation, New York, pp. 29–33.

Longuet-Higgins, M.S., 1970. Longshore currents generated by obliquely incident sea waves, 1. J. Geophys. Res. 75, 6778–6789.

Longuet-Higgins, M.S., Stewart, R.W., 1964. Radiation stress in water waves, a physical discussion with application. Deep Sea Res. 11, 529–563.

McKee, S., Mitchell, A.R., 1970. Alternating direction methods for parabolic equations in two space dimensions with a mixed derivative. Comput. J. 133, 81–86.

McKee, S., Wall, D.P., Wilson, S.K., 1996. An alternating direction implicit scheme for parabolic equations with mixed derivative and convective terms. J. Comput. Phys. 126, 64–76.

Noyes, J.T., Guza, R.T., Feddersen, F., 2005. Model–data comparisons of shear waves in the nearshore. J. Geophys. Res. 110, C05019. doi:10.1029/2004JC002541.

Oberhuber, J.M., 1993. Simulation of the Atlantic circulation with a coupled sea ice-mixed layer-isopycnal general circulation model. Part I. Model description. J. Phys. Oceanogr. 23, 808.

Özkan-Haller, H.T., Kirby, J.T., 1999. Nonlinear evolution of shear instabilities of the longshore current: a comparison of observations and computations. J. Geophys. Res. 104 (C11), 25,953–25,984.

Putrevu, U., Svendsen, I.A., 1999. Three-dimensional dispersion of momentum in wave-induced nearshore currents. Eur. J. Mech. B, Fluids 18, 83–101.

Sancho, F.E., Svendsen, I.A., 1998. Shear waves over longshore nonuniform barred beaches. Proc. 26th Int. Conf. on Coast. Engrg., Copenhagen, pp. 230–243.

Shchepetkin, A.F., McWilliams, J.C., 2005. The regional oceanic modeling system (ROMS): a split-explicit, free-surface, topography-following-coordinate oceanic model. Ocean Model. 9, 347–404.

Shi, F., 2007. CoastGrid, a software for curvilinear grid generation. Report No. CACR-07-01. Cent. for Appl. Coastal Res., Univ. of Del., Newark, Del.

Shi, F., Dalrymple, R.A., Kirby, J.T., Chen, Q., Kennedy, A., 2001. A fully nonlinear Boussinesq model in generalized curvilinear coordinates. Coast. Eng. 42, 237–258.

Shi, F., Svendsen, I.A., Kirby, J.T., Smith, J.M., 2003. A curvilinear version of a quasi-3D nearshore circulation model. Coast. Eng. 49, 99–124.

Smith, R., 1997. Multi-mode models of flow and of solute dispersion in shallow water. Part 3. Horizontal dispersion tensor for the velocity. J. Fluid Mech. 352, 331–340.

Svendsen, I.A., Putrevu, U., 1994. Nearshore mixing and dispersion. Proc. Roy. Soc. Lond. A 445, 561–576.

Svendsen, I.A., Haas, K., Zhao, Q., 2002. Quasi-3D nearshore circulation model SHORECIRC. CACR Report No. CACR-02-01. Cent. for Appl. Coastal Res., Univ. of Del., Newark, Del.

Taylor, G.I., 1953. Dispersion of soluble matter in solvent flowing slowly through a tube. Proc. Roy. Soc. Lond. A 219, 186–203.

Taylor, G.I., 1954. The dispersion of matter in a turbulent flow through a pipe. Proc. Roy. Soc. Lond. A 219, 446–468.

van Dongeren, A.R., Svendsen, I.A., 2000. Nonlinear and 3D effects in leaky infragravity waves. Coast. Eng. 41, 467–496.

Warming, R.F., Beam, R.M., 1979. An extension of A-stability to alternating direction methods. BIT 19, 395–417.

Wei, G., Kirby, J.T., 1995. A time-dependent numerical code for the extended Boussinesq equations. J. Waterw. Port Coast. Ocean Eng. 121 (5), 251–261.

Yu, J., Slinn, D.N., 2001. Effects of wave–current interaction on rip currents. J. Geophys. Res. 108 (C3), 3088. doi:10.1029/2001JC001105.

Zhao, Q., Svendsen, I.A., Haas, K.A., 2003. Three-dimensional effects in shear waves. J. Geophys. Res. 108 (C8), 3270. doi:10.1029/2002JC001306.